Synthesis of CCVJ-Sia for the Biodetection of Siglec Receptors

National Chiayi Senior High School, Taiwan
Students: Bo-Ru Wu, Kuang-Hui Ho
Supervisor: Ruei-Ding Hung

Abstract:

Fluorescent probes are powerful tools for real-time, sensitive imaging. However, conventional probes emit continuously, which generates background noise and compromises accuracy. Fluorogenic probes overcome this limitation by remaining non-emissive until activated by environmental triggers, thereby enhancing imaging contrast, specificity, and biomarker selectivity. This strategy is particularly valuable in renal cancer, which is often diagnosed at advanced stages and lacks effective diagnostic tools. In this work, we focused on abnormal sialylation and Siglec overexpression[1] as rational design principles for targeted fluorogenic probes[2].

We successfully synthesized CCVJ-Sia, a julolidine-based fluorogenic probe conjugated with a sialic acid moiety for active targeting. The key step—direct glycosylation with 6-azidohexan-1-ol—was achieved using a ball-mill-assisted, solvent-minimized mechanochemical method. The identity of CCVJ-Sia was confirmed by HRMS with the observed m/z 657.3147 and further characterized by ^{1}H NMR spectroscopy. Upon excitation at 430 nm, CCVJ-Sia exhibited a maximum fluorescence emission around 500 nm. Fluorescence studies revealed viscosity-dependent turn-on emission consistent with the TICT mechanism. In cell-based assays, CCVJ-Sia selectively illuminated PANC-1 (Siglec-positive) cells but not HepG2 (Siglec-negative) cells, validating its specificity and biological relevance.

Graphical abstract:

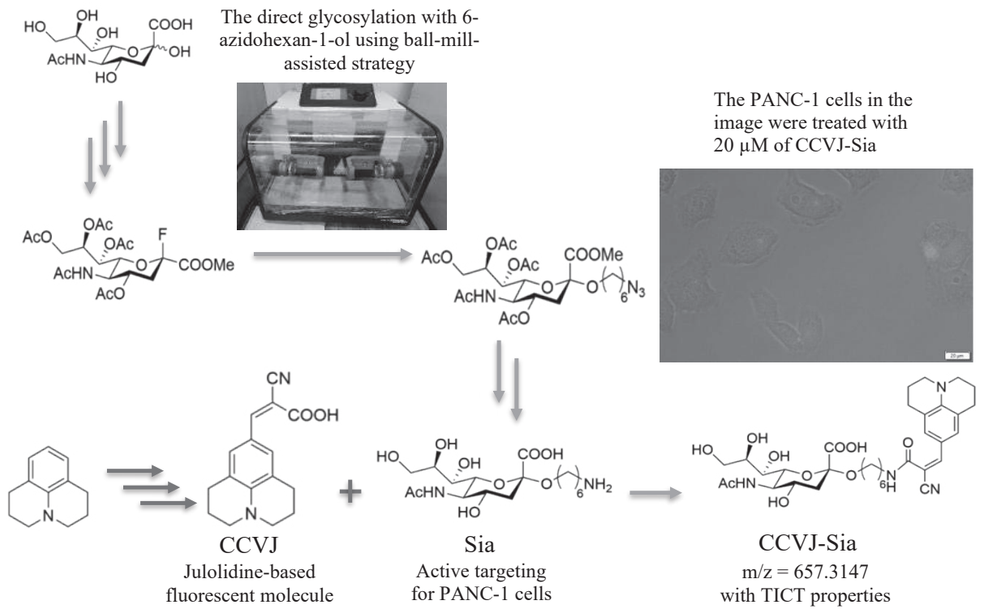

1. Introduction

Fluorescent probes are important tools in biomedical imaging and diagnostics due to their high sensitivity, rapid readout, and real-time visualization of cellular processes. Despite these advantages, conventional probes such as methylene blue and DAPI fluoresce continuously, regardless of target binding. This indiscriminate emission generates background signals, lowering the signal-to-noise ratio and limiting detection accuracy. To address this limitation, researchers have developed environment-sensitive fluorogenic probes, which remain non- or weakly emissive until activated by environmental changes such as binding or conformational restriction. This "turn-on" response effectively reduces background interference and enhances imaging contrast. One established strategy to achieve such responsiveness is the twisted intramolecular charge transfer (TICT) mechanism, in which fluorescence intensity is coupled to local factors like viscosity or molecular interactions.

Here we synthesized CCVJ-Sia, a julolidine-based fluorogenic probe conjugated with a sialic acid moiety for active targeting. The overall synthesis of CCVJ-Sia is shown in Scheme 1. The key step—the direct glycosylation with 6-azidohexan-1-ol (from compound **7** to compound **8**)—was achieved using a ball-mill-assisted, solvent-minimized mechanochemical method. The identity of CCVJ-Sia was confirmed by HRMS and ^{1}H NMR spectroscopy. We also investigated the fluorescence properties, especially viscosity-dependent turn-on emission consistent with the TICT mechanism. Finally, we conducted cell-based assays, in which CCVJ-Sia selectively reacted with target cells, thereby confirming its specificity and biological relevance.

Scheme 1. The Synthesis of CCVJ-Sia

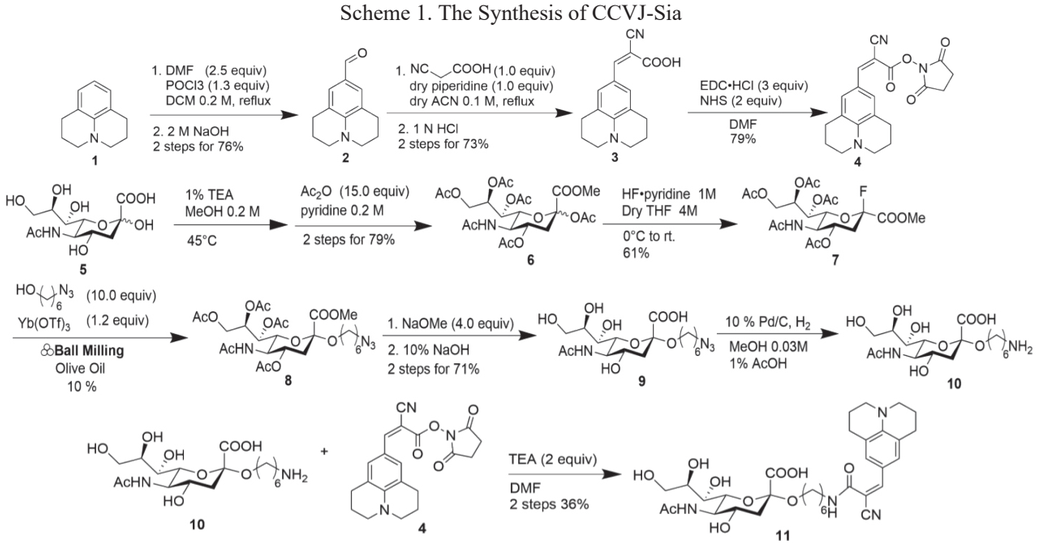

2. Experimental Methods

2.1. The direct glycosylation with 6-azidohexan-1-ol

Compound **8** was prepared by adding 120 mg compound **7**, 343.6 μL (10 eq.) $HO(CH_2)_6N_3$, as well as 18 μL olive oil, together with a zirconia ball (Φ 10 mm) as the milling medium, into a ball-milling container made of ZrO_2, followed by the addition of $Yb(OTf)_3$. The container was placed in a ball-milling machine and milled at 17 Hz for 4 h. The residue was extracted with $NaHCO_{3\,(aq.)}$/EtOAc as well as H_2O/EtOAc to remove all the soluble reaction products. The organic phase was washed with saturated brine, dried over Na_2SO_4, filtered, and

concentrated *in vacuo*. The residue was then purified by silica gel chromatography to afford compound **9** (60.6 mg, 10%).

2.2 The Synthesis of fluorophore CCVJ-Sia (compound **11**)

A solution of 30.6 mg compound **10** in 0.5 mL anhydrous DMF was added to a flask containing 14.6 mg of compound **4** and 24 μL of triethylamine (TEA). The reaction mixture was stirred for 1 h, and completion was confirmed by TLC analysis. The mixture was concentrated in vacuo and purified by silica gel chromatography to afford 20.0 mg of compound **11**.

3. Results and Discussion

3.1. The synthesis and characterization of CCVJ-Sia

CCVJ-Sia is a julolidine-based fluorogenic probe conjugated with a sialic acid moiety for active targeting. We first synthesized the fluorescent moiety and the recognition moiety separately, then combined the two parts to obtain the target probe. The synthetic strategy for CCVJ-Sia is depicted in Scheme 1.

9-(2-carboxy-2-cyanovinyl)julolidine (CCVJ), an iconic fluorophore with TICT properties, was prepared from julolidine (compound 1) through the Vilsmeier–Haack reaction followed by the Knoevenagel condensation[4]. NHS was then introduced to improve reactivity for subsequent amide bond formation with glycoside. *N*-acetylneuraminic acid (sialic acid) was selected as the glycan scaffold. Glycosylation was carried out via a ball-mill-assisted strategy[3] after appropriate protection and C-1 functionalization. This solvent-minimized method offers high reproducibility and operational simplicity compared with conventional low-temperature procedures, thereby reducing synthetic complexity. Compound 4 and compound 10 were conjugated to form our target product—CCVJ-Sia.

^{1}H NMR and HRMS analyses were performed to confirm the successful synthesis of our target compound—CCVJ-Sia. Signal integrations and characteristic chemical shifts match the expected structure (Figure 1). High-resolution mass spectrometry verified the molecular formula, with the observed m/z 657.3147, matching the theoretical value of 657.3136 within 0.17 ppm.

Figure 1. ^{1}H NMR spectrum of CCVJ-Sia.

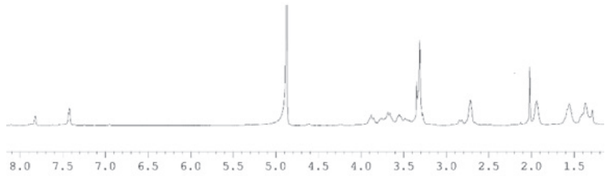

Next, we investigated whether the probe retained turn-on/off switch with TICT characteristic by dissolving the probe in solvents of different viscosities. Upon excitation at 430 nm, CCVJ-Sia exhibited a maximum fluorescence emission around 500 nm in DMF, DMSO, glycerol or glycerol/water mixtures (Table 1).

	solvent 1	solvent 2	solvent 3	solvent 4	solvent 5	solvent 6	solvent 7
solvent composition	glycerol/water = 2/1	glycerol/water = 1/1	glycerol/water = 1/2	glycerol	DMF	DMSO	toluene 96.7% in DMF
slovent viscocity η(cP)	945	30	8	1200	0.92	1.996	0.59
wavelength (nm)	503.8	504.2	503.2	500.6	491	502.4	578
relative intensity I	2166	954.4	629.5	5892	384.9	885.7	345.1
log(η)	1.48	0.9	0.3	3.08	-0.04	0.3	-0.23
log(I)	3.34	2.98	2.80	3.77	2.59	2.95	2.54

Table 1. Fluoresce studies of CCVJ-Sia in different solvents under λ_{ex} = 430 nm.

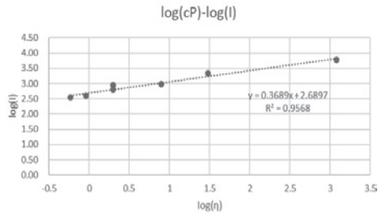

Figure 2. Log-log plot of FL intensity (I) of CCVJ-Sia as a function of fluid viscosity (η).

Through fluorescence spectrophotometry, under 430 nm excitation wavelength, the probe emitted fluorescence that fit the Förster–Hoffmann equation ($\log I = C + x \log \eta$) with a correlation coefficient of 0.962 (Figure 2). A linear relationship between the logarithm of fluorescence intensity and the logarithm of viscosity was consistent with TICT theory.

3.2. Cellular Assays of CCVJ-Sia

Cellular assays were performed to verify whether the probe could bind to Siglecs. Preliminary cell tests using HepG2 and PANC-1 cells showed green fluorescence only in PANC-1, which express Siglecs. (Figure 3) This suggests the probe binds to Siglecs, restricting probe twisting and enhancing fluorescence as intended for screening. Low background interference was observed, as fluorescence was only seen in cells. These results highlight CCVJ-Sia as a promising low-background probe despite being structurally simpler than most probes and support the feasibility of utilizing sialic-acid-presenting probes as a new method for biological detection of renal cell carcinoma (RCC), the most common form of kidney cancer.

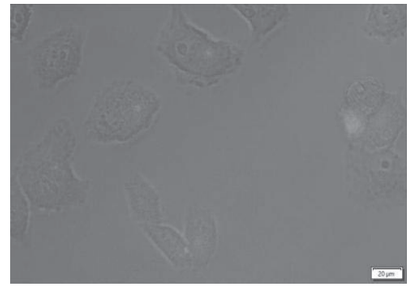

Figure 3. The PANC-1 cells in the image were treated with 20 μM of our probe dissolved in aqueous PBS. The green areas indicate fluorescence.

4. Conclusion and Perspective

We synthesized CCVJ-Sia, a julolidine-based fluorogenic probe bearing a sialic acid moiety, via a solvent-minimized ball-mill glycosylation strategy. The approach provided a straightforward and greener route to the key intermediate, and the product was verified by ^{1}H NMR and HRMS.

CCVJ-Sia displayed viscosity-dependent turn-on fluorescence consistent with the TICT mechanism and followed the Förster–Hoffmann relationship, confirming its environment-sensitive nature. In cellular assays, the probe selectively lit up Siglec-expressing PANC-1 cells while remaining silent in Siglec-negative HepG2 cells, demonstrating both low background and target specificity. These findings point toward CCVJ-Sia as a proof of concept for combining smart chemistry with targeted biology, enabling sensitive detection of Siglec receptors, potentially applying to the detection of renal cancer cells and guiding the future development of glycan-based diagnostic probes.

5. References

(1) Ou, L.; Liu, J.; Wang, S.; Dai, Y.; Qu, Y.; Xiong, W.; Xi, J.; Xu, J.; Guo, X. *Urol. Oncol.* 2017, 35 (10), 607.e1–607.e8.

(2) Li, P.-J.; Kawade, S. K.; Adak, A. K.; Shen, Y.-J.; Fan, C.-Y.; Hsieh, Y.-H.; Angata, T.; Chen, Y.-J.; Lin, C.-C. *J. Chin. Chem. Soc.* 2022, 69 (8), 1326–1337.

(3) Ruan, B.-C.; Li, C.-H.; Chang, H.-E.; Li, P.-J. *Chem. Asian J.* 2025, 20 (3), e202401130.

(4) Varejão, J. O. S.; Varejão, E. V. V.; Fernandes, S. A. *Eur. J. Org. Chem.* 2019, 27, 4273–4310.

Development of Phosphine-Catalyzed *β*-Acylation Reaction: Synthesis of Diketopyrrolidine Derivative

Taipei First Girls High School, Taiwan

Students: Wu, Tzu-Ting, Chang, Chia-En

Supervisor: Yao, Yueh-Yun

Abstract:

The development of efficient and versatile acylation strategies remains a significant challenge in synthetic organic chemistry, particularly in constructing pharmacologically relevant scaffolds. In this study, we focused on the realization of a demanding ***β*-acylation reaction** to furnish products with **pyrrolidine-2,3-dione** structural framework which has promising potential as an **Alzheimer's disease inhibitor**. To achieve this transformation, the trifluoromethyl unit from **trifluoroacetic anhydride** was introduced, and a selected **organic phosphine** reagent was employed as the catalyst. Systematic optimization of the reaction conditions, together with mechanistic investigations, enabled us to establish a solid theoretical foundation for β-acylation and to broaden its applications in **drug-oriented synthesis**.

Graphical abstract:

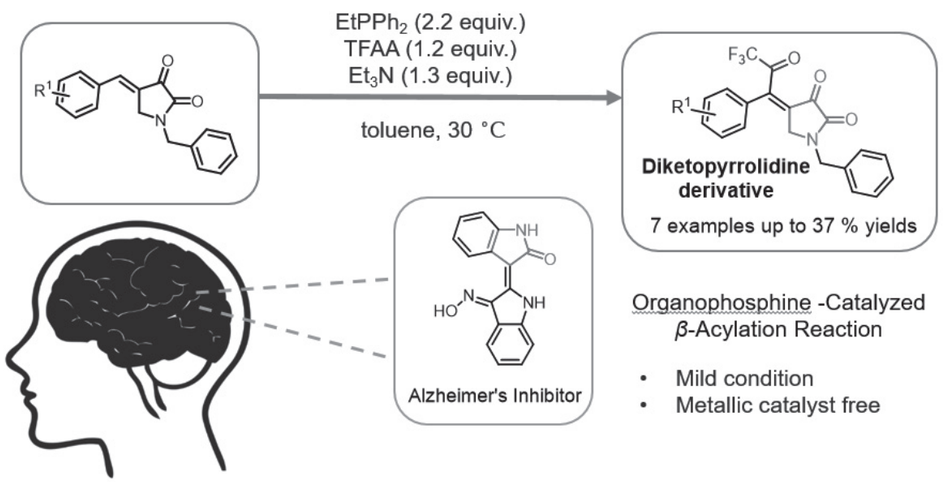

1. Introduction

Pyrrolidine-2,3-dione is a key scaffold in Alzheimer's disease drug development, and synthesizing new derivatives remains an important direction for therapeutics. However, addition reactions between like-charged functional groups are typically challenging, and conventional metal catalysts are often costly and environmentally unfavorable.

To overcome these limitations, we developed a novel β-acylation reaction using trifluoroacetic anhydride, with an inexpensive and eco-friendly organophosphine reagent as a catalyst. This approach proceeds efficiently at room temperature, broadens the scope of organic synthesis, and provides a versatile route to generate new 2,3-dione derivatives with relevance to Alzheimer's drug development.

2. Experimental Methods

2.1 General procedure of Organophosphine -Catalyzed *β*-Acylation

The reactions were carried out with starting material **1**, **1a**, **1b**, **1c**, **1d**, **1e**, **1f** (0.2 mmol), $EtPPh_2$ (2.2 equiv.), TFAA (1.2 equiv.), Et3N (1.3 equiv.) in anhydrous toluene (2.0 mL) under argon atmosphere at 30 °C. Remaining of **1**, **1a**, **1b**, **1c**, **1d**, **1e**, **1f** was determined by ^{1}H NMR analysis of the crude reaction mixture using Ph_3CH as an internal standard. Yield of product **2**, **2a**, **2b**, **2c**, **2d**, **2e**, **2f**, was determined by ^{1}H NMR analysis of the crude reaction mixture using $CHPh_3$ as an internal standard.

2.2 Instrument analysis

Analytical thin layer chromatography (TLC) was performed on precoated alumina-backed silica gel plates (Merck 60 F254, 0.2 mm thickness) which were developed using UV irradiation at 254 nm. ^{1}H NMR spectra were recorded on either an Oxford JEOL 400 MHz spectrometer or a Bruker Ascend 400 MHz spectrometer, ^{13}C NMR spectra at 100 MHz or 150 MHz, ^{31}P NMR at 162 MHz and ^{19}F NMR at 376 MHz. Chemical shifts are reported in δ ppm referenced to an internal TMS standard (δ = 0.0 ppm) for ^{1}H NMR, CDCl3 (δ = 77.0 ppm) for ^{13}C NMR. High resolution mass spectra were recorded on Waters XeVo G2-S QTof using ESI (TOF analyzer).

3. Results and Discussion

3.1 Optimization the condition of Organophosphine -Catalyzed *β*-Acylation

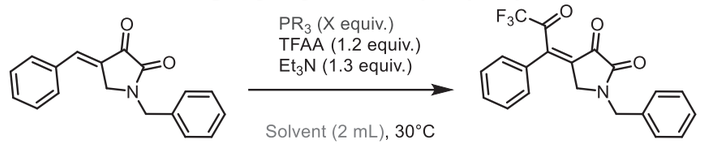

1 **2**

Entry	PR_3	Equivalent of PR_3	Solvent	Time (h)	Remaining **1** (%)	Yield **2** (%)
1	PPh_3	1.1	DCE	5 min/ 1/ 2	23/ 28/ 25	trace
2	$MePPh_2$	1.1	toluene	5 min/ 1/ 2	21/ 25/ 24	24/ 27/ 28
3	$MePPh_2$	1.1	THF	5 min/ 1/ 2	61/ 68/ 62	6/ 5/ 5
4	$MePPh_2$	1.1	DCE	5 min/ 1/ 2	16/ 15/ 17	14/ 15/ 17
5	$EtPPh_2$	1.1	toluene	5 min/ 1/ 2	24/ 22/ 22	20/ 15/ 15
6	$EtPPh_2$	1.1	THF	5 min/ 1/ 2	79/ 69/ 60	trace
7	$EtPPh_2$	1.1	DCE	5 min/ 1/ 2	29/ 28/ 28	20/ 15/ 17
8	PBu_3	1.1	toluene	5 min/ 1/ 2	50/ 49/ 50	trace
9	$MePPh_2$	0.3	toluene	5 min/ 1/ 2	46/ 80/ 80	trace

10	$MePPh_2$	2.2	toluene	5 min/ 1/ 2	16/ 10/ 9	27/ 31/ 32
11	$EtPPh_2$	0.3	toluene	5 min/ 1	45/ 38	trace
12	$EtPPh_2$	2.2	toluene	5 min/ 1/ 2	trace	36/ 37/ 35

We found that the use of $MePPh_2$ and $EtPPh_2$ as organophosphine reagents in anhydrous toluene afforded higher yields (entry 1, 4, 7, and 8). The relatively high nucleophilicity of $MePPh_2$ and $EtPPh_2$, together with the electron-donating and steric effect of the organophosphines, facilitated the 1,4-addition required to initiate the subsequent transformations.

We further discovered that non-protic solvents were more suitable for this reaction. In particular, the use of a less polar solvent such as toluene, combined with $MePPh_2$ as the phosphine reagent (entry 2), provided the most favorable reaction conditions.

Although the organophosphine reagent plays the role of a catalyst in the *β*-acylation reaction, lowering the amount of phosphine to a catalytic level did not afford the target product. Instead, the reaction required an equimolar amount of the phosphine reagent relative to the starting material, suggesting that the phosphine might be consumed by side reactions. Therefore, we increased the loading of the phosphine reagent as a variable in our condition optimization. Notably, when 2.2 equivalents of $EtPPh_2$ were employed, the yield reached 37%.

3.2 Substrate scope

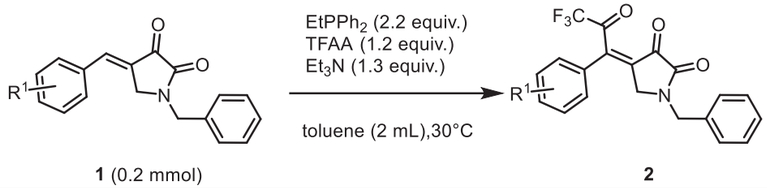

1 (0.2 mmol) **2**

Entry	R^1	Time (h)	Remaining (%)	Yield (%)
1	H	5min/ 1/ 2	trace	36/ 37 /35
2	4-Br	5min/ 1/ 2	45/ 31/ 47	10/ 18/ 19
3	3-Br	5min/ 1/ 2	trace	31/ 32/ 33
4	2-Br	5min/ 1/ 2	21/ 18/ 18	trace
5	4-OMe	5min/ 1/ 2	23/ 13/ 14	8/ trace/ trace
6	2-Naphth	5min/ 1/ 2	trace	12/15/15
7	4-NO_2	5min/ 1/ 2	10/ 14/ 14	15/ 22/ 12

From the proposed reaction mechanism, when the carbocation on the starting material is sufficiently stabilized, the phosphine reagent can more effectively add to this reactive site, thereby driving the reaction forward. Thus, in our investigation of substituent effects, we focused on how different substituents influence the charge distribution at the *β*-position of the starting material.

In the case of bromine substituents on the phenyl ring (4-Br, 3-Br, and 2-Br), the electron-withdrawing effect of bromine, the electronic properties of the aromatic ring, and steric hindrance all influenced the stability of the β-carbocation, leading to different effects on the reaction yield. Among these, the 3-Br substituent provided the highest yield.

When a strong electron-donating substituent was introduced, as in the case of the 4-OMe group, the yield decreased significantly. This result suggests that the electron-donating ability of the methoxy group reduced the positive charge at the *β*-position of the starting material, thereby weakening the reactivity and resulting in

a lower yield. Finally, we also examined heteroaryl substitutions, which were found to cause a further decrease in yield.

3.3 Plausible Mechanism

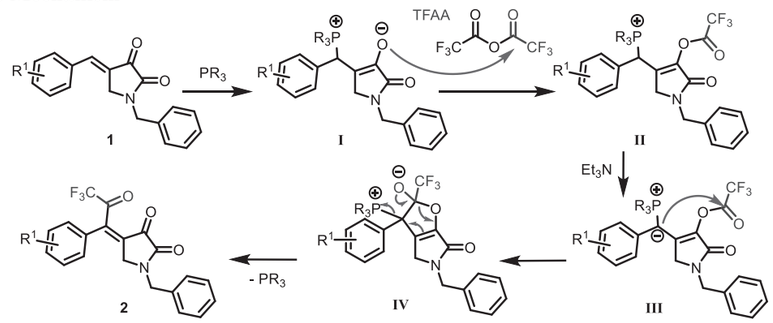

According to our study, a plausible reaction mechanism was proposed. First, the addition of the phosphine reagent to the *β*-position of the starting material took place, giving the corresponding intermediate. In the second step, the acylation reagent reacted with the negatively charged oxygen atom. Then, deprotonation by the base occurred, followed by electron transfer and intramolecular cyclization, affording the target product.

4. Conclusion and Perspective

The optimized *β*-acylation reaction currently achieves a maximum yield of 37%. We successfully synthesized and purified several phosphonium salt intermediates, which provide strong evidence for our proposed reaction mechanism and confirm the catalytic role of the organophosphine reagent.

Unlike traditional metal-catalyzed coupling reactions for C-C bond formation, a key achievement of this study is the direct construction of a C-C single bond between two electron-deficient carbon atoms. In this study, we overcame the synthetic challenge and successfully prepare the target product. Future work will focus on further optimizing the reaction to employ only catalytic amounts of the organophosphine reagent, thereby improving atom economy. We also plan to further derivatize the product to generate a broader range of derivatives with potential applications.

5. References

1) Lee, C., Sheu, C., Tsai, C., Wu, Z., & Lin, W. (2014). Direct β-Acylation of 2-Arylidene-1,3-Indandiones with Acyl Chlorides Catalyzed by Organophosphanes . Chem. Commun., 50, 5304-5306

2) Yang, S., Wang, C., Lin, C., Karanam, P., Reddy, G. M., Tsai, Y., & Lin, W. (2018).Diversity-Oriented Synthesis of Furo[3,2-c]Coumarins and Benzofuranyl Chromenones through hemoselective Acylation/Wittig Reaction. Angew. Chem. Int. Ed. 57, 1668 –1672

3) Luo, Z., Sun, G., Wu, S., Chen, Y., Lin, Y., Zhang, L., & Wang, Z. (2021, May 28). η 6 -Arene CH−O Interaction Directed Dynamic Kinetic Resolution – Asymmetric Transfer Hydrogenation (DKR-ATH) of A-Keto/Enol-Lactams.

4) Zeb, A., Kim, D., Alam, S. I., Son, M., Kumar, R., Rampogu, S., ... & Lee, K. W. (2019). Computational simulations identify pyrrolidine-2, 3-dione derivatives as novel inhibitors of Cdk5/p25 complex to attenuate Alzheimer's pathology. Journal of Clinical Medicine, 8(5), 746.

Investigation of the wound healing and antibacterial properties of chitosan-bromelain and gelatin-bromelain composite nanofibers

Hwa Chong Institution, Singapore
Ku Jun Kai, Yu Zhuohang
Supervisor: Kong Chiak Wu

Abstract:

Chemical burns are a major cause of mortality, with infections often leading to sepsis and delayed healing. This study developed electrospun chitosan–bromelain (ChBr) and gelatin–bromelain (GeBr) nanofibers composites to evaluate their antibacterial and wound-healing potential. Chitosan was extracted from prawn shells (degree of deacetylation: 67.6%) and blended with bromelain and polyethylene oxide to produce nanofibers via electrospinning. The resulting nanofibers were characterised using SEM and FT-IR. SEM revealed a porous fibrous structure, while FT-IR confirmed the successful incorporation of bromelain into both chitosan and gelatin matrices. Antibacterial activity was assessed against *E. coli* and *S. epidermidis* and wound-healing efficacy was tested in a *Tenebrio molitor* (mealworm) chemical burn model. ChBr nanofibers produced significantly larger zones of inhibition than GeBr nanofibres (Mann–Whitney U test, $p = 0.00107$), indicating synergistic antibacterial activity between chitosan and bromelain. In the burn wound model, ChBr nanofibers significantly prolonged survival compared to Ch, Ge, and GeBr groups ($p < 0.05$). The enhanced efficacy of ChBr nanofibers is attributed to chitosan's intrinsic antimicrobial properties, its stabilisation of bromelain, and its ability to promote fibroblast proliferation and tissue regeneration. Overall, ChBr nanofibers demonstrated superior antibacterial activity and wound-healing performance, highlighting their suitability as wound dressings for burn treatment.

Graphical abstract:

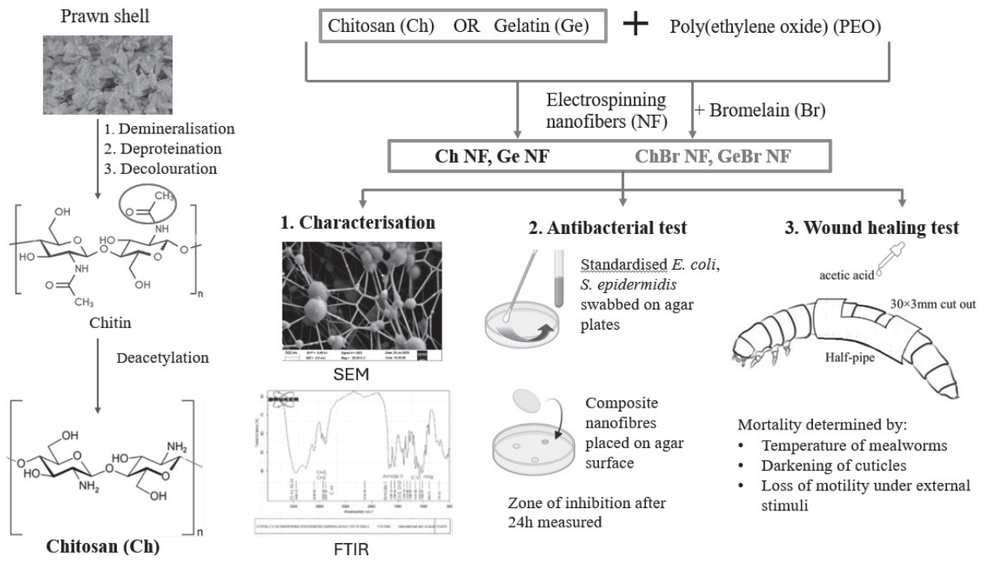

1. Introduction

Burn wound infections are a major cause of mortality, accounting for over half of burn-related deaths, with chemical burns causing disproportionately high fatalities. In this study, Tenebrio molitor (mealworm) was employed as a burn model to evaluate the therapeutic potential of electrospun nanofibers composites made from gelatin, gelatin–bromelain, chitosan, and chitosan–bromelain. We hypothesise that chitosan–bromelain nanofibers will demonstrate superior wound healing and antibacterial effects compared to gelatin–bromelain nanofibers, leading to reduced mortality and stronger inhibition of bacterial growth.

2. Experimental Methods[1,3,4]

Green synthesis of chitosan. The sample was washed in boiling water and dried at 60°C. The sample was treated with a 10% (w/v) HC*l* solution for 24h, washed repeatedly until pH neutral and oven dried. It was then treated with 2% (w/v) NaOH solution and refluxed at 60°C for 4h, followed by washing until pH neutral. The samples were then stirred in sodium hypochlorite at room temperature for 24h, filtered and dried at 60°C until constant mass. Chemical deacetylation from chitin to chitosan was achieved by refluxing extracted chitin in 50% (w/v) sodium hydroxide for 65h at 70°C with a solid to solvent ratio (w/w) of 1:5. The resulting chitosan was then washed until pH neutral and dried.

Synthesis of composite nanofibers (NF). Chitosan (5% w/v) and gelatin (5% w/v) were dissolved in acetic acid, while bromelain (20% w/v) and PEO (2.5% w/v) were dissolved in deionised water. ChBr and GeBr solutions were prepared by mixing 8 m*l* polymer solution with 1 m*l* bromelain and 1 ml PEO; Ch and Ge solutions were prepared with the same formulation but excluded bromelain. Mixtures were stirred at 60°C for 2 h. Electrospinning used a 0.9 mm needle, 12 kV voltage, and 120 mm needle-to-collector distance onto silicone-coated aluminum foil at room temperature.

Antibacterial test of composite nanofibers. Gram-negative *E. coli* and Gram-positive *S. epidermidis* were each incubated in 10 m*l* Luria–Bertani broth overnight at 37°C. Müeller–Hinton agar plates were prepared, bacterial cultures were standardised to similar OD_{600} values before being swabbed evenly onto agar plates. Wells (6 mm) were loaded separately with ChBr or GeBr nanofibers discs, 80μ*l* of 10% (w/v) bleach (positive control), or sterile deionised water (negative control). Plates were incubated at 30°C overnight, and zones of inhibition were measured.

Chemical burn wound healing test. Each Tenebrio molitor (mealworm) was covered with a half-pipe featuring a 30×3 mm cutout, and 30 μ*l* of 2.5% (w/v) acetic acid was applied to the exposed skin for 10 s before removing the half-pipe. A 30×3 mm composite nanofiber was then placed on each mealworm. Seven mealworms were housed per 90 mm Petri dish lined with filter paper and 1 m*l* deionised water, replenished daily, and incubated at room temperature for 120 h. Mortality was assessed using an infrared thermometer, cuticle darkening, and lack of response to stimuli. Seven replicates were conducted per test.

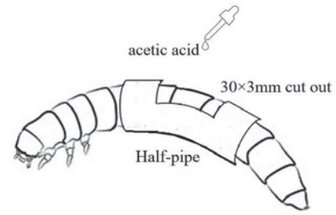

3. Results and Discussion

SEM analysis (Fig. 1) showed that nanofibers exhibited porous structure with a high surface-area-to-volume ratio, consistent with previous reports on nanofibers for wound healing scaffolds. Such morphology is desirable for biomedical applications. However, nodular formations were observed along the fibers, which may compromise their effectiveness in wound healing. Due to time constraints, further optimisation of the nanofiber morphology could not be pursued in this study.

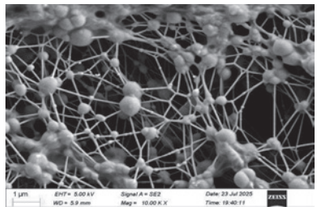

Fig. 1 SEM image of Ch-Br nanofibres

The FT-IR results (Fig. 2) verified the successful conversion of chitin into chitosan. In chitin, the strong amide I band (C=O stretching) is split into two components at 1660 and 1625 cm^{-1}, whereas in chitosan this band appears as one component at 1657 cm^{-1}, reflecting structural modification during deacetylation[1]. The amide II band at 1556 cm^{-1}, characteristic of N–H bending in the acetamide group, disappeared completely in the chitosan spectrum, confirming the removal of acetyl groups. In addition, a new band emerged at 1422 cm^{-1}, for CH_2 bending/CH_3 deformation, further supporting the formation of free amino groups[1]. The degree of deacetylation (DD) of the synthesized chitosan was determined to be 66.6% using FT-IR spectroscopy (calculated with the formula DD (%) = [1 − (A1655/A3450)/1.33] × 100) and 67.6% using acid–base titration. Both results are consistent with the typical range of deacetylation reported for chitosan, further confirming that chitin was successfully converted to chitosan[2].

Incorporation of bromelain into the chitosan matrix was confirmed by FT-IR of ChBr nanofiber. The spectrum of the composite exhibited characteristic amide I and II bands of bromelain (1636 and 1540 cm^{-1})[4]. The FT-IR spectrum of the GeBr nanofiber exhibits the characteristic peaks of both gelatin and bromelain, confirming the successful incorporation of bromelain.

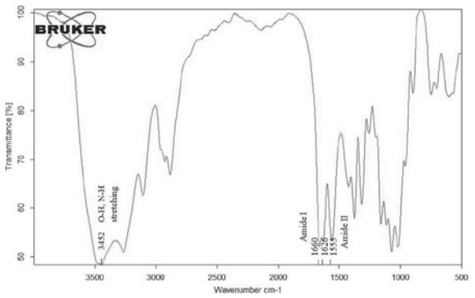

FTIR spectrum of chitin

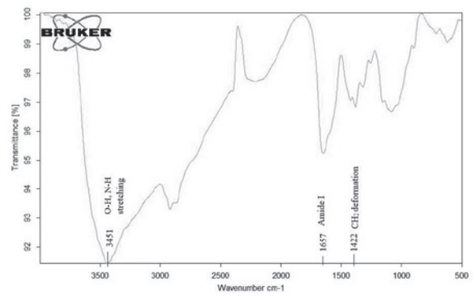

FTIR spectrum chitosan

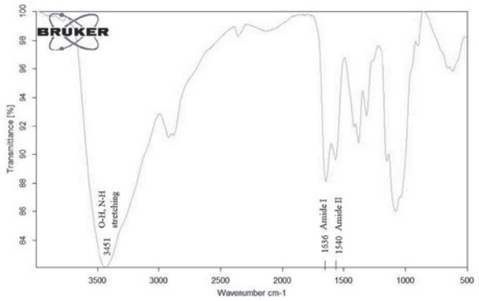

FTIR spectrum of ChBr nanofibers

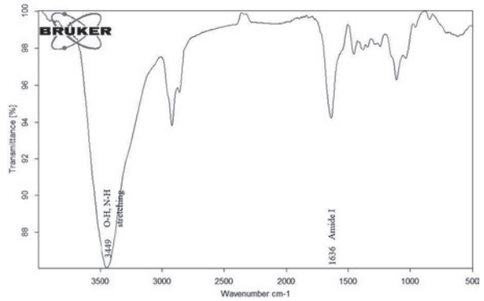

FTIR spectrum of GeBr nanofibers

Fig. 2 FTIR spectra of chitin, chitosan, GeBr nanofibres and ChBr nanofibers

The antibacterial activity of the nanofibers was evaluated using the zone of inhibition assay (Fig. 3). GeBr nanofibers produced zones of 6 mm (*E. coli*) and 4 mm (*S. epidermidis*), whereas ChBr nanofibers showed significantly larger zones of 12 mm and 13 mm, respectively. Positive controls exhibited 19 mm (*E. coli*) and 20 mm (*S. epidermidis*). Mann–Whitney U tests confirmed that the superior antibacterial activity of ChBr over GeBr was statistically significant for both strains (p = 0.00107), indicating a synergistic effect between chitosan and bromelain. Chitosan disrupts bacterial membranes via electrostatic

interactions, while bromelain proteolytically degrades surface proteins, producing broad-spectrum antibacterial activity against Gram-negative *E. coli* and Gram-positive *S. epidermidis*[4,5].

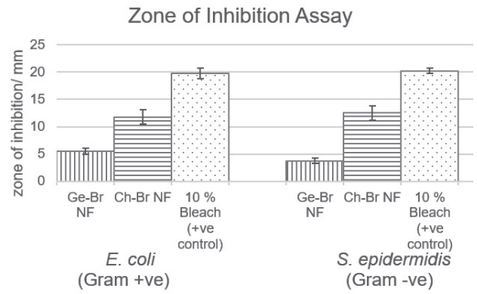

Fig. 3 Zone of inhibition assay

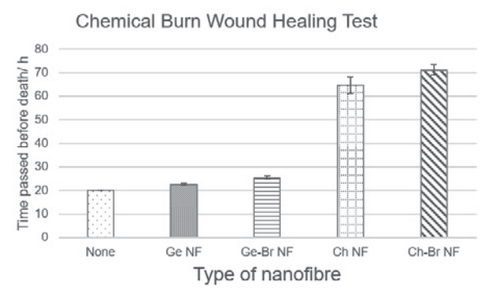

Fig. 4 Chemical burn wound healing test

In the chemical burn wound healing test, untreated mealworms survived 20 h, gelatin nanofibers 22 h, GeBr 25 h, and Ch nanofibers 64 h. ChBr nanofibers extended survival to 71 h. Chitosan greatly prolonged the survival of mealworms from 20 h to 64 hr. Statistical analysis revealed that ChBr outperformed Ch (p = 0.0126) and GeBr (p = 0.0107), demonstrating significant synergistic effects of chitosan and bromelain. The enhanced wound healing of ChBr nanofibers is attributed to chitosan's antimicrobial properties, bromelain's proteolytic and anti-inflammatory actions, stabilization of bromelain within the chitosan matrix, and the high surface area of the nanofibrous structure, facilitating localized delivery and tissue repair[3,4,5]. Gelatin-based nanofibers lack these combined functionalities, resulting in comparatively slight improvements.

4. Conclusion and Perspective

ChBr nanofibers outperformed GeBr, Ch, and Ge nanofibers in both antibacterial activity and wound healing, demonstrating synergistic effects of chitosan and bromelain. All nanofibers exhibited some antibacterial properties, but ChBr showed the highest efficacy against Gram-positive and Gram-negative bacteria. These findings highlight bromelain-containing composite nanofibers as a promising alternative to conventional plasters. Future studies should assess long-term cytotoxicity, biocompatibility, sustained bromelain release, physical properties, and antibacterial effectiveness against additional bacterial strains.

5. References

1. Tolaimate, A., El Gharous, M., & El Gharous, M. (2015). Preparation and characterization of chitosan obtained from shrimp shells. *Journal of Materials Science and Engineering B, 5*(1), 1–7.
2. Peh, K. K., & Khan, T. A. (2002). Chitosan: An evaluation of its pharmaceutical properties. *Journal of Pharmacy & Pharmaceutical Sciences, 5*(3), 205–212.
3. Liu, Y., & Bai, X. (2009). Chitosan kills bacteria through cell membrane damage. *International Journal of Food Microbiology, 134*(3), 101–105.
4. Santos, M. A., & Silva, A. M. (2022). Antimicrobial properties of chitosan from different developmental stages of *Tenebrio molitor*. *Scientific Reports, 12*(1), 1–12.
5. Pavan, R., Jain, S., Shraddha, & Kumar, A. (2012). *Properties and therapeutic application of bromelain: A review.* Biotechnology Research International, 2012, Article 976203.

Improved Method for Chitosan Extraction from Cicada Sloughs and Evaluation of its Solubility at various pH and Biodegradability in Soil

Kajonkietsuksa School, Thailand

Students: Worakit Ploysri

Supervisor: Peerapong Meesin

Abstract:

The rising demand for sustainable biomaterials has promoted the use of insect waste as a renewable resource. This study optimized the extraction of chitin and chitosan from cicada sloughs and evaluated film degradability in aqueous and soil environments. The modified method overcame pigmentation issues, yielding 25.96% chitin that was decolorized to off-white and deacetylated to chitosan with a degree of deacetylation of 95.38 ± 2.37%. Films prepared from 1% and 3% (w/v) chitosan showed distinct properties: the 3% film was thicker, stronger, and more yellowish, while the 1% film was thinner and more flexible. Solubility tests (pH 3–13) revealed faster dissolution for the 1% film, with both dissolving under acidic conditions and remaining insoluble at pH ≥ 11. In soil, the 1%w/v chitosan film degraded by day 2 and the 3%w/v chitosan film by day 3. These findings confirm cicada-derived chitosan as a high-purity, low-molecular-weight material with rapid biodegradability, highlighting its potential for biomedical and sustainable packaging applications.

Graphical abstract：

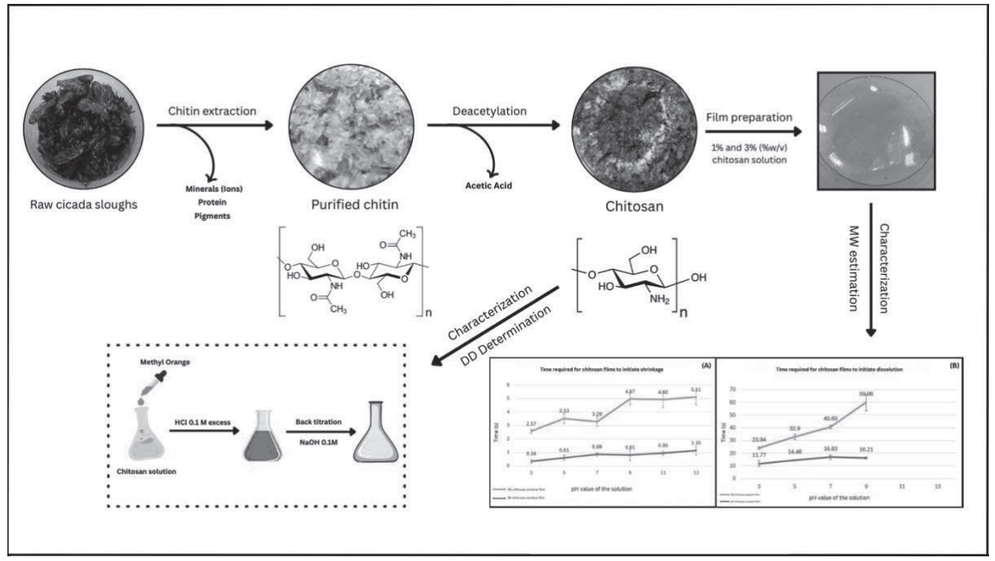

1. Introduction

Plastics are widely used but their persistence leads to global pollution and ecological harm. As alternatives, insect-derived biopolymers such as chitin and chitosan are attracting interest for their biodegradability and versatility. Cicadas, abundant in Thailand, leave behind discarded exuviae rich in α-chitin, which can serve as a renewable source. Compared with crustacean shells, insect cuticles require milder processing, though existing protocols often produce impure products. In this study, I introduce a modified extraction method to improve quality and reliability of chitin and chitosan from cicada sloughs. Chitosan, derived from chitin by alkaline deacetylation, is soluble in dilute acids, positively charged, antimicrobial, and film-forming, supporting its applications in agriculture, cosmetics, and biomedicine. Its properties depend mainly on molecular weight (MW) and degree of deacetylation (DD), which influence solubility, bioactivity, and film strength. Here, I prepare chitosan films from two concentrations and evaluate their solubility across pH 3–13 and biodegradability in soil, providing insights into their potential as sustainable bioplastic alternatives.

2. Experimental Methods

Chitin extraction and deacetylation to chitosan. Cicada sloughs were pre-treated by soaking in 75% ethanol, rinsing, and drying at 60 °C overnight. Chitin was extracted following a modified protocol: ground samples were sequentially demineralized with 1 M HCl, deproteinized with 1 M NaOH under reflux, and decolorized using 2% $KMnO_4$, 2% oxalic acid, and 35% H_2O_2, with drying and weighing after each step. The resulting chitin was deacetylated with 60% NaOH at 100 °C for 8 h to yield chitosan, which was washed to neutrality and dried.

Characterization of chitin and chitosan. Chitin and chitosan were characterized by visual color assessment, yield determination at each extraction stage, and degree of deacetylation (DD or DDA) using acid–base titration, which is calculated using the given equation:

$$DDA\ (\%) = 100\frac{(203.19\ \mathrm{g/mol} \times \Delta V \times [NaOH])}{m + (42.03\ \mathrm{g/mol} \times \Delta V \times [NaOH])}$$

Where, ΔV refers to V_{HCl}−V_{NaOH}. 203.19 g/mol corresponds to the molecular weight of the N-acetyl glucosamine monomer. 42.03 g/mol is the molecular weight difference between N-acetyl-glucosamine and D-glucosamine monomer. Briefly, 20.00 mL of 1M HCl were pipetted into an Erlenmeyer flask containing 0.20g chitosan product. 13-14 drops of methyl orange were added into the solution as an indicator. 0.1M NaOH were used as a titrant. Record the consumed volume of NaOH when the color of the solution turned from pink to yellow. Titration were performed in triplicate for accuracy.

Film fabrication and characterization. Chitosan films were prepared by dissolving 0.50 g or 1.50 g of chitosan in 50 mL of 1% or 3% acetic acid, respectively, casting onto Petri dishes, drying at room temperature for two days, and oven-drying at 35°C for 2 h to improve film integrity. Film characterization included visual color evaluation, thickness measurement in triplicate using a micrometer (0–25 mm, 0.001 mm precision), solubility testing in pH 3–13 solutions by recording the onset of swelling and shrinkage, and biodegradability testing by burying film samples (2 × 2 cm, triplicates) in garden soil for seven days with daily observations.

3. Results and Discussion

As summarized in Figure 1, Cicada sloughs were processed into chitin and chitosan with clear morphological changes. Raw samples (A and B) were brownish, demineralization lightened the color (C), deproteinization smoothed the surface (D), and decolorization produced off-white chitin (E). Deacetylation yielded yellowish-white flakes (F), confirming chitosan formation. The chitin yield was 25.96%, while chitosan was lower at 11.45% (44.11% of chitin mass), likely due to depolymerization during harsh alkaline treatment. According to Table 1, an acid–base titration revealed a mean degree of deacetylation (95.38 ± 2.37%), which lies in the range of an ultra high DD value, signifying high purity and abundant free amino groups that enhance solubility and functionality.

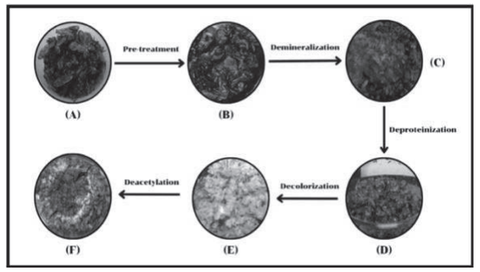

Figure 1 Morphological changes observed during extraction process

Replicate	Consumed NaOH volume (mL)	Measured %DD
1	8.41	94.69
2	8.60	93.43
3	7.90	98.01
Mean ± SD (%DD)	8.30 ± 0.36	95.38 ± 2.37

Table 1 Determination of the degree of deacetylation of obtained chitosan by acid-base titration

Chitosan films were successfully prepared from 1% and 3% acetic acid solutions (Table 2 and Figure 3). The 1% film was thin, transparent, and flexible, while the 3% film appeared thicker, stiffer, and less transparent. Solubility testing across pH 3–13 (Figure 2) showed both films dissolved rapidly at acidic to neutral pH (3–9), with the 1% film degrading faster, whereas the 3% film maintained structure longer. Neither dissolved at pH ≥ 11, confirming chitosan's insolubility in alkaline media. Rapid dissolution in acidic solutions suggests relatively low molecular weight material.

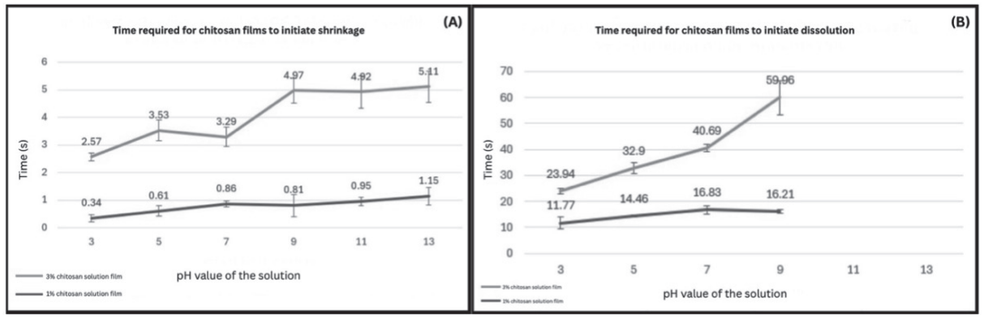

Figure 2 Comparison between time required for initial shrinkage and dissolution in various pH solution of films from 1% and 3% chitosan solution

Film property	1% chitosan film	3% chitosan film
Color	Colorless, transparent	Yellowish, translucent
Thickness (mm)	0.035 ± 0.006	0.144 ± 0.025
Tensile strength	Lower	Higher
Solubility	Higher	Lower
Biodegradability	Higher	Lower

Table 2 Comparison of Physical, Mechanical, and Chemical Properties between 1% and 3% (w/v) Chitosan Films

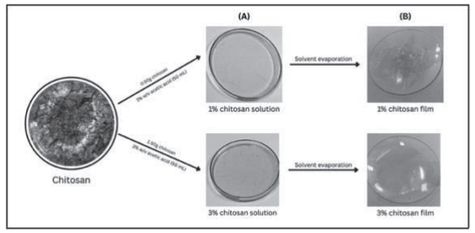

Figure 3 Physical appearance of chitosan sample during film formation process

Film Type	Replicate 1	Replicate 2	Replicate 3	Average Day to Initial Shrinkage
1% Chitosan	Day 2	Day 2	Day 2	Day 2
3% Chitosan	Day 3	Day 3	Day 3	Day 3

Table 3 Biodegradation timeline of Chitosan Films in the garden soil

Soil burial confirmed biodegradability (Table 3). The 1% film degraded by Day 2, while the 3% film resisted visible breakdown until Day 3, reflecting greater density and slower microbial attack. Overall, cicada slough-derived chitosan provided films with tunable solubility and degradation profiles, highlighting their potential as sustainable bioplastic alternatives for packaging and biomedical use.

4. Conclusion and Perspective

Chitin was successfully extracted from cicada sloughs under mild conditions, with decolorization yielding an off-white product. Conversion to chitosan was confirmed by acid–base titration, showing a high degree of deacetylation. Films made from higher chitosan concentrations were thicker, stronger, and more yellowish, but less soluble and slower to degrade. Solubility and biodegradation patterns suggest relatively low molecular weight chitosan, likely influenced by processing. This combination of high DD and low molecular weight enhances solubility and bioactivity, making it suitable for applications such as drug delivery and cosmetics. Future work should optimize processing to better control molecular weight and tailor material properties.

5. References

1) Sajomsang, W.; Gonil, P. Preparation and Characterization of α-Chitin from Cicada Sloughs. Materials Science and Engineering: C **2010**, 30 (3), 357–363. https://doi.org/10.1016/j.msec.2009.11.014.

2) Ons Amamou; Kefil, S.; Denis, J.-P.; Taoufik Boubaker; Cardinal, S. Revisiting the Determination of the Degree of Deacetylation Using Potentiometric Titration: A New Equation for Modified Chitosan. *Molecules* **2024**, *29* (13), 2962–2962. https://doi.org/10.3390/molecules29132962.

3) Sogias, I. A.; Khutoryanskiy, V. V.; Williams, A. C. Exploring the Factors Affecting the Solubility of Chitosan in Water. Macromolecular Chemistry and Physics **2009**, 211 (4), 426–433. https://doi.org/10.1002/macp.200900385.

IP-05

Reducing air pollution by turning carbon dioxide into oxygen using cyanobacteria

Atast, Tunisia

Student: Rana Boukadida

Supervisor: Hatem Slimane

Abstract:

Air pollution is a serious environmental problem mainly caused by the high amounts of CO2 emission that's why this project's aim is to decrease the volume of this gas in the air

This approach is based on a chemical reaction called photosynthesis of cyanobacteria which role is to absorb co2 from the atmosphere and produce oxygen .By using our device we will produce the optimal results of this reaction by manipulating many physical variables such as humidity, temperature, light intensity and exposure using solar energy

And many other factors are important to keep the best results like ph level, liquid concentration and nutrients availability

This IOT approach will collect the real time data through its sensors analyze it then send it to the user's application and inform him of the co2 volume reduced by litre and alert him in case of abnormal activity

This device will be extremely practical by taking the form of tables in open space cafes supplied with charging ports

Graphical abstract:

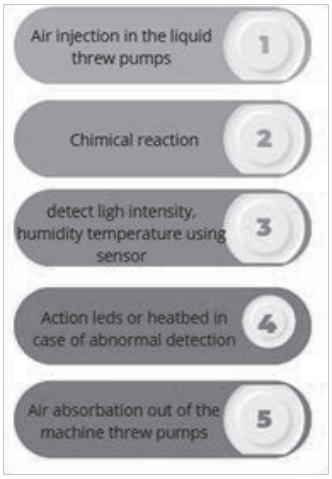

Figure 1 : General steps

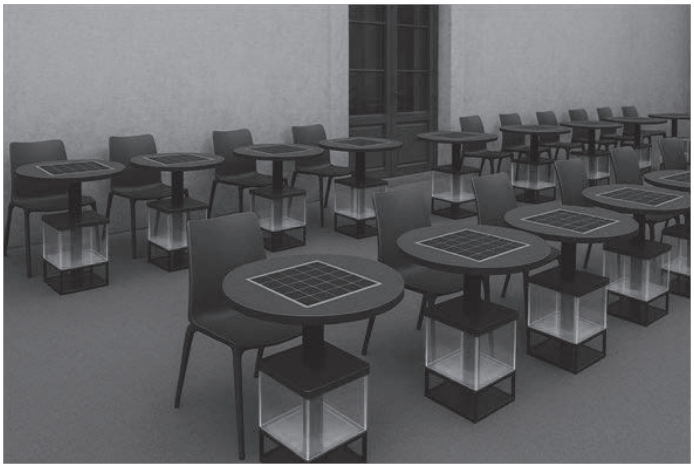

Figure 4 : 3D design of the overlook of the devices